International Journal of Science and Research (IJSR)
ISSN: 2319-7064
SJIF (2020): 7.803

Geothermal Potential Mapping Using Landsat 8 OLI and TIR Data in Northern Sector of Main Ethiopian Rift

Talema Reda[*1], Worku Gebrehiwot[2], Zeleke Anteneh[3], Yared Abraha[4]

[1]Department of Geology, Arba Minch University, P.O. Box 21, Arba Minch, Ethiopia
Corresponding Author's Email Address: *talema.moged[at]amu.edu.et*

[2, 4]Department of Remote Sensing Research and Development, Ethiopian Space Science and Technology Institute(ESSTI), P.O. Box 33679, Addis Ababa, Ethiopia

[3]Department of Geology, Wollo University, P.O. Box 1145, Dessie, Ethiopia

Abstract: ***Ethiopia has a significant amount of geothermal resources distributed throughout the Main Ethiopian Rift. However, the potential areas of exploration have not been yet supported through geospatial technology for geothermal power-plant development. Hence this study assess geothermal potential areas using remote sensing technology over the northern segment of the Main Ethiopian Rift. Emissivity Modulation method (EM) was adopted to retrieve surface kinetic temperature anomalies using Landsat 8 Operational Land Imager (OLI) and the Thermal Infrared Sensor (TIRS). The surface kinetic temperature resulted with a minimum and maximum value of 21 and 45.9 ^{0}C respectively. Furthermore, the surface kinetic temperature is reclassified into categories to identify geothermal fields. The spatial distribution of surface kinetic temperature was computed with hydrothermally altered grounds derived from atmospherically corrected surface reflectance images using band ratio analysis. The highest surface temperature anomalies were found in the region of highly faulted areas, active volcanic landforms, hot springs, mud pools, fumaroles, steaming grounds and hydrothermally altered grounds. Based on the result of this study and field investigation economically feasible geothermal resource areas were found mainly in the location of Fantale volcano. Less pronounced geothermal potential areas were found near to Kone volcanic complex and Boseti volcano.***

Keywords: Emissivity Modulation Method, Geothermal potential, Landsat 8, Mapping, Surface kinetic temperature

1. Introduction

Remote sensing technology can be used as cost-effective tools in geothermal exploration activities to map large spatial areas [29, 32, 43, 46, 54, 56]. Thermal infrared (TIR) images are able to sense geothermal activity for supporting the exploration activities [13, 17, 82]. These thermal images have been widely used to explore surface features above geothermal reservoirs that are obviously hot and less obvious surface attributes of geothermal fields [22, 58]. It also potentially very useful in outlining surface temperature anomalies and geothermal gradient related to geothermal resources [13, 17, 61]. Thermal bands enable obtaining land surface temperature (LST) as they measure the emitted energy of the land surfaces. Hence, the surface temperature of large areas can be quickly assessed and the location of active geothermal manifestations and the distribution of thermal anomaly accurately identified using thermal bands [33]. As per previous studies, satellite imagery such as Landsat 5 Thematic Mapper(TM), Landsat 7 Enhanced Thematic Mapper (ETM+) and Landsat 8 thermal infrared (TIRS) sensors have been widely used for estimating land surface temperature and geothermal anomalies [7,67]. The land surface temperature was computed using various methods such as Mono-Window, Single-Channel, Split-Window algorithm, Emissivity Modulation and Radiative Transfer Equation [52, 53, 65].

Ethiopia is currently widening alternative renewable energy resources such as hydropower, biomass, solar, geothermal, and wind energy to replace fossil fuels. From these resources government of Ethiopia planned to increase electricity generation capacity by installing a geothermal power plant which is seasonally independent and unlimited energy source. The geothermal resources of Earth are more than the energy demand for electricity generation [62]. About 1% of geothermal energy is equivalent to about 500 times energy obtained from fossil fuels [25]. However, the current electricity generation capacity from geothermal energy is less than 1% due to limited attempt of developing the industry owing to the difficulty in identifying potential targets using only ground surveys.

This study aimed to assess the spatial distribution of surface kinetic temperature anomalies for the identification of geothermal potential areas in the northern volcanic segment of the Main Ethiopian Rift. The study has a significant contribution to support an early study conducted in Kone and Fantale geothermal prospects using ground surveys. The government of Ethiopia is planning to explore more than 60MW geothermal energy in the study area [38]. Therefore, the output of this study is believed to offer detailed information about the spatial distribution of geothermal potential sites and develop scientific theory.

2. Literature Review

Geothermal energy is heat energy generated and stored in the interior of the earth's layers. It is one of the most promising renewable energy sources available in the Earth's crust and is clean, plentiful, reliable, sustainable, and environmentally sound with various applications in modern

energy sectors [13, 36]. The geothermal resources include dry steam, hot water, hot dry rocks, magma and ambient ground heat [66].

The main sources of geothermal energy in the earth's crust are radiogenic heat formed from radioactive decay, original heat formed immediately after the formation of infant earth, potential heat formed during the formation of the new crust and fractional energy generated during the occurrence of an earthquake [51]. The largest heat source of the earth's crust is generated from radioactive decay of minerals (80%) and 20% obtained from original heat, potential heat and frictional energy [20, 51, 62, 85].

As far as the issue of various volcano-tectonic factors, geothermal systems occur at the surface of the earth's crust associated with high crustal heat flux that may be related to the occurrence of young igneous bodies or hot rocks located deeper in the crust [21, 29, 64]. It can also be situated in the region with normal or slightly above normal geothermal gradient [75] and this is always occurring in the region of plate margin such as convergent, and divergent plate [13,45].

The Main Ethiopian Rift ispart of the divergent plate boundaries in which the respective plates are diverging away from each other [6]. It is one of the major volcanically and tectonically active regions in the world [12, 40, 80]. Though Ethiopia has a huge geothermal potential resource distributed throughout the rift, its development is lagging behind [39, 79].

3. Materials and Methods

3.1 Study Area

The study area is located in the northern segment of Main Ethiopian Rift Valley which covers part of Bosset, Fantale, and Minjar-Shenkora districts found in North Shewa zone of Amhara regional state and East Shewa zone of Oromia regional state. The study area is dominated by the Boseti-Kone and Fantale volcanic fields which are found in the district of Melka-jilo and Metehara town. It is bounded within a longitude of 8.59 to 9.14 degrees and latitude of 39.45 to 40.00 degrees and covering an area of about 2447km^2.

The study area is mainly covered by barren land and lava flows. The vegetation cover is typical of arid and semi-arid climate zones, with scattered acacia, mainly thorn bushes, and shrubs. Acacia and scrubs are dominant along the streams, Lakes, and ridge sides. The vegetation cover is dense on the younger volcanic area and less on the ignimbrites and ash-flow tuffs. There are modern mechanized farms located to the south of Fantale volcano, near to Lake Beseka namely; Metehara and Abadir farms which are the largest agro-industrial complex of the country. To the north of Fantale there is also Saboure plantation and this farm grows fruits (banana and mango), sugar cane, and cotton[9].The geology of the study area includes aphyric flood basalts associated with rhyolite, ignimbrites, subordinate trachyte and basalts transitional to tholeiitic in nature, pumice, ash, peralkaline lavas, pyroclastic deposit, obsidian flows, tuff, scoriaceous basalt eruptions, basaltic flows, scoria cones, basaltic hyaloclastites and alluvium products(silt, sand, and clay) [9, 77]. Those rock units exposed on the study area are varies based on their isotopic date, degree of weathering and effect of active faults. Since the study area is affected by two distinct system of normal faults namely: boundary faults and Wanji Fault Belt. The boulder faults are characterized by long, widely spaced,large offset faults that give rise to the major escarpments separating the rift floor from the plateaus. However, the Wonji Fault Belt faults are short in length and closely spaced with small offsets [3, 4].

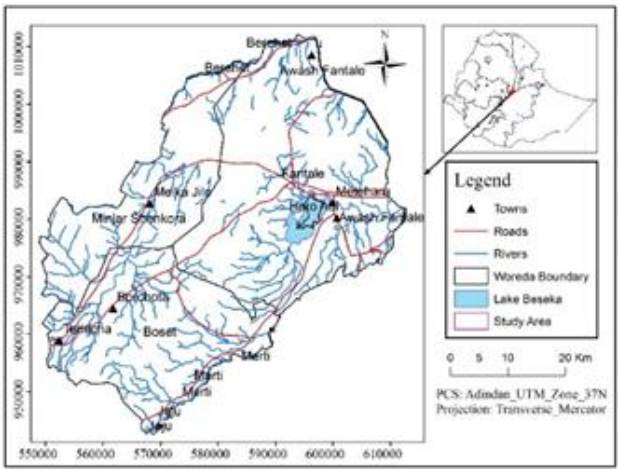

Figure 1: Location of study area

3.2 Data

Landsat 8 imagery acquired on 16 January 2019 was used for this study. Landsat imagery was obtained from United States Geological Survey (USGS) portal with path and row 168 and 054 respectively. The Landsat-8 level-1 product contains nine spectral bands and two thermal bands. The thermal infrared band is affected by stray light. The differences between the ground-based surface temperature and thermal infrared results ranged up to 5 Kelvin in the thermal infrared band 10 and up to 10-Kelvin in thermal infrared band 11 [81]. For correlation and validation of surface kinetic temperature calculated from Landsat 8 TIR sensor, daytime average 8-day per-pixel LST products of MODIS (MOD11A2) with a 1-kilometer spatial resolution was acquired from the same portal at a path and row of 168 and 054 respectively.

3.3 Methods

3.3.1 Data Preprocessing

The OLI bands are largely contaminated by the atmospheric conditions [81]. Radiometric and atmospheric correction were performed to retrieve the real surface parameters by removing the atmospheric effects such as absorption, scattering of the radiation from the earth's surface, and upward emission [19]. The radiometric correction of the OLI and TIRS sensors involves rescaling the raw digital numbers transmitted from the satellite to a calibrated digital number which have the same radiometric scaling for all scenes processed on the ground for a specific period [14]. The DN converted to spectral radiance employing the following

equation using the radiance scaling factors provided in the metadata file [81].

$$L_\lambda = ML_\lambda x Q_{Cal} + A_L \ldots\ldots\ldots\ldots\ldots\ldots\ldots (1)$$

Where Lλ is the Spectral radiance (W/ (m2 * sr * μm)), ML is the multiplicative radiance value, A_L is the additive radiance value and Q_{Cal} is the pixel values in DN.

Table 1: OLI and TIRS bands constant values used to estimate radiance [81]

Bands	Multiplicative Radiance	Additive Radiance
Band 4	0.010326	-51.62814
Band 5	0.0063188	-31.59385
Band 10	0.00033420	0.10000

Conversion of radiance to surface reflectance is essential for Landsat 8 OLI spectral bands to estimate Normalized Difference Vegetation Index (NDVI), Vegetation Proportion (V_P), and Land Surface Emissivity of the study area. In this study, the Fast Line of sight Atmospheric Analysis of Spectral Hypercubes (FLAASH) atmospheric correction model was used to remove the influence of atmospheric particles. The FLAASH atmospheric correction model is a computational radiation transfer algorithm used to model the spectral absorption, transmission, emission, and scattering of atmospheric particles [34]. It is also an advanced atmospheric correction model based on the Moderate Resolution Atmospheric Transmission (MODTRAN4) algorithm, carried out in FLAASH module in ENVI software version. It is a first-principles atmospheric correction tool that incorporates with the MODTRAN4 radiation transfer code and used to correct wavelengths in the visible and near-infrared regions up to 3μm. The FLAASH is used to compute a scene average visibility such as aerosol or haze amount, adjust spectral polishing for artifact suppression, handling the presence of clouds, and correct pixel mixing due to scattering of surface-reflected radiance [23]. In addition, the Min Noise Fraction (MNF) rotation is followed by an inverse transform to produce spectral images that are relatively free from noise. The MNF transformation is performed using ENVI software version 5.2 after FLAASH atmospheric correction. The MNF transformation is used to obtain true surface reflectance by removing residual noise from the reflectance image [57].

3.3.2 Calculation of Land Surface Emissivity

Land surface emissivity is the main factor that affects the accuracy of surface kinetic temperature retrieved from satellite imagery. It is a proportional factor that scales blackbody radiance (Plank's law) to predict emitted radiance and is the efficiency of transmitting thermal energy across the surface into the atmosphere [72]. It is the emitting ability of a real material as compared to that of a black body and is a spectral property that varies with the composition of the material and the geometric configuration of the surface. The emissivity values of the non-black body vary between 0 and 1 [59]. In this sense, land surface emissivity is used to estimate surface kinetic temperature from radiance measurements. Different approaches have been used to estimate land surface emissivity from NDVI values [83]. In this study, $NDVI^{THM}$ method is used, which is first developed and applied to Advanced Very High-Resolution Radiometry (AVHRR) data and later compared with other methods and adapted to other sensors [70]. It is also employed for the estimation of surface emissivity from Landsat imagery. In $NDVI^{THM}$ method the statistical relationship between NDVI and emissivity over thermal infrared spectral bands is used to determine land surface emissivity.

Land surface emissivity is calculated from $NDVI^{THM}$ values considering three different land cover classes [69,72, 86]. In the first case, NDVI< 0.2, the pixel is considered as bare soil and the emissivity is obtained from reflectance values in the red region. In the second case, 0.2≤ NDVI≤ 0.5, the pixel is composed of a mixture of bare soil and vegetation and in the third case, NDVI> 0.5, the pixel is considered as a fully vegetated area. Due to the occurrence of various land cover classes in the study area, the mixed pixel of 0.2 ≤ NDVI ≤0.5 was selected to estimate land surface emissivity. This is considered as the mixture of soil and vegetation cover and applied to estimate land surface emissivity of the study area according to equation (2). The land surface emissivity values of soil and vegetation must be known to calculate land surface emissivity using a mixed pixel equation.

$$\varepsilon_\lambda = \begin{cases} a_\lambda \rho_R + b_\lambda NDVI < NDVI_S, \\ \varepsilon_{V\lambda} P_V + \varepsilon_{S\lambda}(1 - P_V) + C_\lambda, \quad NDVI_S \le NDVI \le NDVI_V, \\ \varepsilon_{S\lambda} + C_\lambda NDVI > NDVI_V \end{cases}$$

……..……..…. (2)

Where, ρ_R is the reflectance value of the red band, aλ and bλ are estimated from an empirical relationship between the red band reflectance and MODIS emissivity library [65].

$$\varepsilon_\lambda = \varepsilon_{V\lambda} P_V + \varepsilon_{S\lambda}(1 - P_V) + C_\lambda \ldots\ldots\ldots\ldots\ldots\ldots (3)$$

Where, $\varepsilon_{V\lambda}$, $\varepsilon_{S\lambda}$ are vegetation and soil emissivity respectively and C_λ is cavity effect due to surface roughness (C_λ=0 for a homogenous and flat surface). The cavity effect for the rough surface (heterogeneous surface) area is calculated as:

$$C_\lambda = (1 - \varepsilon_{S\lambda})(1 - P_V)\varepsilon_{V\lambda} F' \ldots\ldots\ldots\ldots\ldots\ldots\ldots (4)$$

Where Cλ is the term that depends on the surface characteristics and which considers the internal reflections(cavity effect), F' is a shape factor whose mean value is ranging between zero and one, depending on the geometrical distribution of the surface. Since the geometrical factor cannot be estimated from a satellite image, whose mean value, assuming different geometrical distributions is 0.55 [70]. The land surface emissivity can be calculated as

$$\varepsilon_\lambda = mP_V + n \ldots\ldots\ldots\ldots\ldots\ldots\ldots\ldots\ldots (5)$$

With

$$m = \varepsilon_{V\lambda} - \varepsilon_{S\lambda} - (1 - \varepsilon_{S\lambda})F'\varepsilon_{V\lambda} \ldots\ldots\ldots\ldots\ldots\ldots (6)$$

$$n = \varepsilon_{S\lambda} + (1 - \varepsilon_{S\lambda})F'\varepsilon_{V\lambda} \ldots\ldots\ldots\ldots\ldots\ldots\ldots (7)$$

The emissivity values of soil and vegetation for Landsat 8 thermal infrared band 10 are given as 0.9668 and 0.9863 respectively [35, 86]. Hence, the land surface emissivity value of mixed pixel was assessed using the following equation (8).

$$\varepsilon_\lambda = 0.9863 P_V + 0.9668(1 - P_V) + C_\lambda, \qquad 0.2 \le NDVI \le 0.5$$

…… (8)

Where 0.9863 is the emissivity values of vegetation and 0.9668 is the emissivity values of soils for Landsat 8 thermal band 10.

P_V is vegetation proportion (also referred to as fractional vegetation cover) which is assessed based on the NDVI values of soil and vegetation [71]. The pixel considered as bare soil has zero vegetation proportion values (P_V=0) and the pixels with dense vegetation have a vegetation proportion value of P_V=1. NDVI values of vegetation and NDVI values of soilsare extracted from the NDVI histogram as the following equation [72].

$$P_V = \left(\frac{NDVI - NDVI_{min}}{NDVI_{max} - NDVI_{min}}\right)^2 \quad \text{..... (9)}$$

Where NDVI is Normalized Difference Vegetation Index, $NDVI_{min}$ is NDVI value of soil, $NDVI_{max}$ is NDVI value of vegetation.

NDVI is a simple numerical indicator used to quantify vegetation by measuring the difference between the near-infrared band and red band in which vegetation strongly reflects and absorbs respectively. The NDVI algorithm was used to estimate NDVI values of each land cover class. The algorithm subtracts the red band (band 4) reflectance values from the NIR band (band 5) for the OLI sensor and divides it by the sum of that band. The estimation of NDVI is essential since the vegetation coverage is the factor for the spatial variation of surface temperature. The value of NDVI always ranges from -1 to 1. However, there is no distinct boundary between each land cover class. The value of NDVI for the water surface is close to -1. On the other hand, the value of NDVI for vegetation is close to +1 [30]. For this study, the results obtained from NDVI analysis are used to estimate vegetation proportion and land surface emissivity of the study area.

$$NDVI = \frac{NIR - Red}{NIR + Red} \quad \text{.....(10)}$$

Where NDVI is Normalized Difference Vegetation Index, NIR is Near Infrared Band

3.3.3 Calculation of Radiant and Surface Kinetic Temperature

The radiant temperature (brightness temperature) of an object is measured at a distance from the object's surface. It depends on various factors such as surface emissivity, thermal properties, rate of heating, actual or surface kinetic temperature of the object, etc. The radiant temperature measured by satellite data is always less than the actual surface temperature of the objects by the factor of $\varepsilon^{1/4}$. For this study, Landsat 8 thermal infrared band 10 imagery was converted from spectral radiance to radiant temperature which is an effective temperature viewed by the satellite sensor under consideration of unit of emissivity [81].

$$T_R = \frac{K_2}{ln\left(\frac{K_1}{L_\lambda} + 1\right)} \quad \text{.....(11)}$$

Where T_R is the radiant temperature in Kelvin, L_λ is the pixel value as radiance, K1 and K2 is a constant value of 774.8853 and 1321.0789 respectively. The radiant temperature in the unit of Kelvin is converted to degrees Celsius as the following:

$$T_R(C^0) = T_R(K) - 273.15 \quad \text{.....(12)}$$

Where T_R (C^0) is the radiant temperature in degree Celsius, T_R (K) is the radiant temperature in Kelvin. Landsat 8 TIR1 (band 10) thermal constant values used to estimate the radiant temperature are K1= 774.8853 and K2= 1321.0789 [81].

Surface kinetic temperature is the kinetic heat of ground objects and is a measure of the amount of heat energy contained in it. The radiations emitted from the surface of the object is measured using thermal infrared bands of Landsat imagery. The thermal infrared remote sensing exploits the fact that everything above absolute zero kelvin emits radiation in the thermal infrared electromagnetic spectrum region with wavelength ranging from 3-5µm and 8-14µm [29]. Moreover, an object that has a temperature above absolute zero kelvin has random particle motion and when these particles collide they emit electromagnetic radiation. The amount of energy radiated from the objects depends on the surface emissivity and kinetic temperature of the objects. The kinetic temperature is mainly affected by heat energy budgets such as active thermal source (hot springs, fumaroles, fires, volcanoes), solar heat, longwave upwelling, and down-welling radiations and heat transfer at the Earth atmosphere and thermal properties of objects including thermal conductivity, specific heat, density, heat capacity, thermal diffusivities and thermal inertia of the objects [47,59]. Surface kinetic temperature is highly correlated to radiant temperature [59]. The radiant temperature for the black body is the same as kinetic temperature but it varies for the nonblack body.So the surface kinetic temperature of the object is estimated using the relation between radiant and kinetic temperature [47,58,59].

$$T_K = \frac{T_R}{\varepsilon_\lambda^{\frac{1}{4}}} \quad \text{..... (13)}$$

Where T_K is surface kinetic temperature, T_R is the radiant temperature in degree Celsius, and ε_λ is land surface emissivity.

3.3.4 Mapping of Geothermal Potential Field

The results of Surface kinetic temperature computed from Emissivity Modulation method are used to map and analyze the spatial distribution of geothermal fields over the study area. The occurrence of higher surface temperature anomalies at the surface of the earths curst indicate that transfer of thermal energy from the interior of the earth layers towards the surface[27,28, 42,84]. This thermal heat transfer from the source to the surface mostly by conduction processes and less pronounced by convection processes due to movement of hot fluid through geological structures [26, 41,42]. In the rift area, the movement of heat makes the temperature to rise with increasing depth in the curst on average of 25 to 30 ^{0}C. The increment in temperature with depth is due to geothermal gradient[26, 42]. The surface kinetic temperature computed from Landsat 8 imagery of OLI and TIR sensors was classified into five subclasses to identify the location of noticeable geothermal potential sites over the study area [18, 58]. However, urban areas or manmade objects affected the rising of surface temperature when viewed by satellites [18,61]. Due to this reason, an artificial thermal influence was considered during noticeable geothermal potential site selection process. An empirical distance of 2000 meters was assigned as the minimum distance from the urban area [19]. The human influences decrease with increasing distance from the urban area. This made it easier to distinguish true thermal activity from false thermal anomalies.

4. Results and Discussions

4.1 Results

4.1.1 Normalized Difference Vegetation Index and Vegetation Proportion

The NDVI map of the study area is indicated in figure 2. The result indicates that the NDVI value ranges from -0.896 to 0.871. NDVI values for Lake Beseka and Kassem Dam located at the northern tip of the mapped area ranges from -0.896 to -0.189. The NDVI value that ranges from -0.188 to 0.164, could be built-up area, barren areas of rock or sand. NDVI values for the mixture of rock or soil and vegetation ranges from 0.165 to 0.517. The NDVI values for vegetation coverand agro-industrial areas are 0.518 to 0.871.The vegetation proportion was calculated using the maximum and minimum NDVI values. As shown in figure 3, the vegetation proportion of the study area ranged from 0 to 1. Zero means that the area is non-vegetated while one indicates that the area was covered by dense vegetation. The higher values of vegetation proportion were found in vegetated areas and agro-industrial zones. On the other hand, the lowest values of vegetation proportion were observed in the region of water body.

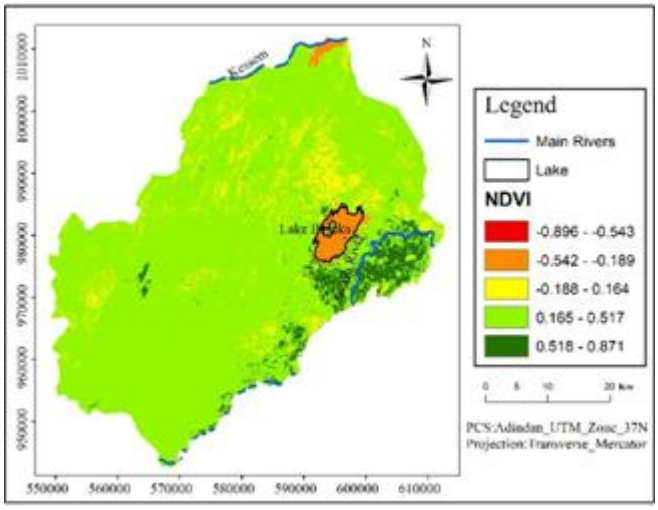

Figure 2: NDVI map of the study area

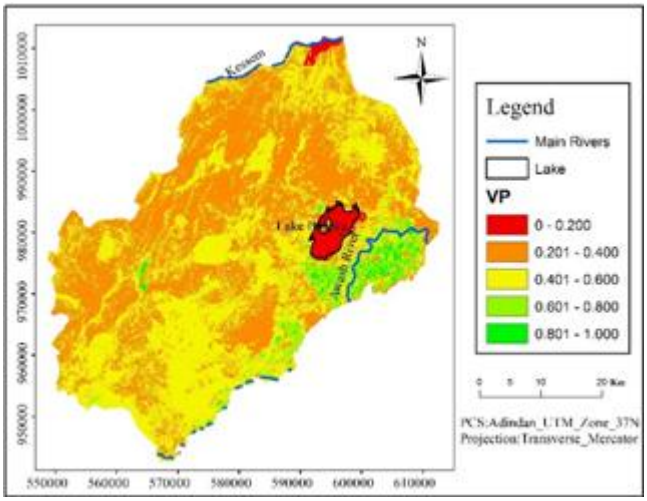

Figure 3: Vegetation proportion map of the study area

4.1.2 Land Surface Emissivity

The land surface emissivity ranged from 0.985 to 0.986. The higher values of land surface emissivity were found in the vegetation covers and agro-industrial areas with direct proportional to higher values of NDVI while the lower values of land surface emissivity were found in the water body of Lake Beseka and Kassem Dam located at the northern tip of the mapped area.

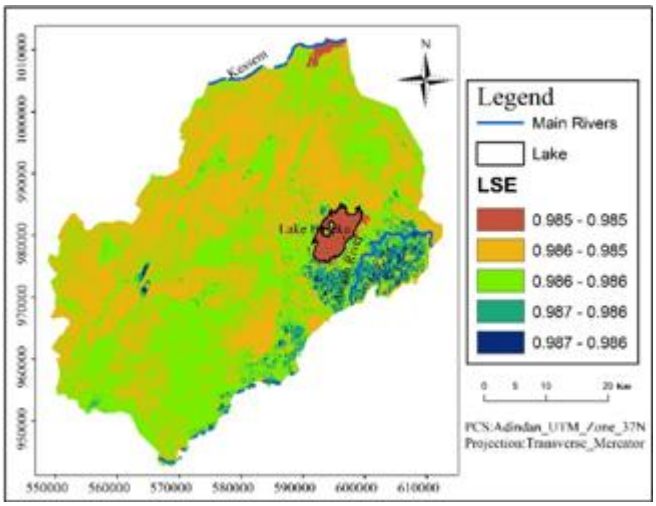

Figure 4: Land surface emissivity map of the study area

4.1.3 Radiant and Surface Kinetic Temperature

The result of radiant and surface kinetic temperature ranges from 21.3 to 45.7^{0}C and 21.0 to 49.9 ^{0}C as shown in figure 5 and 6 respectively. The radiant and surface kinetic temperature has a direct relationship as shown in figures 5 and 6. The variation was observed due to nonblack bodies which have different thermal properties, composition and geometric surface configuration. The variation of surface temperature was observed between various land cover classes ranging from 21.0 to 45.9 ^{0}C. Surface kinetic temperature for Metehara agro-industrial zone and vegetation cover areas range from 21.0 to 32.0^{0}C. In the lava flown areas, the temperature ranges from 32.1 to 38.0^{0}C while bare soil and rock surface and urban areas have a temperature range of 38.1 to 44.0^{0}C. The temperature anomalies reach locally above 44.0^{0}C in Fantale volcanic fields located northeast and north of Lake Beseka and in the area of volcanic domes, cones and higher faults zone along the northeastern and southeastern direction following the rift axis. The land cover types also influence the spatial distribution of surface kinetic temperature. The Lake Beseka, Kessem Dam and Metehara agro industrial area had a lower surface temperature as compared to lava flow area, bare soil surfaces and urban areas. The bare soil surface and urban areas show higher surface temperature than the lava flow areas. Moreover, the area of volcanic domes, cones and highly faulted zone show very high surface temperatures as compared to other land cover classes.

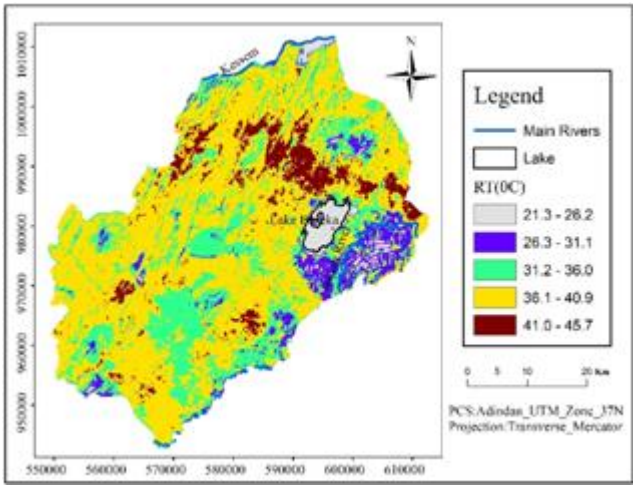

Figure 5: Radiant temperature map of the study area

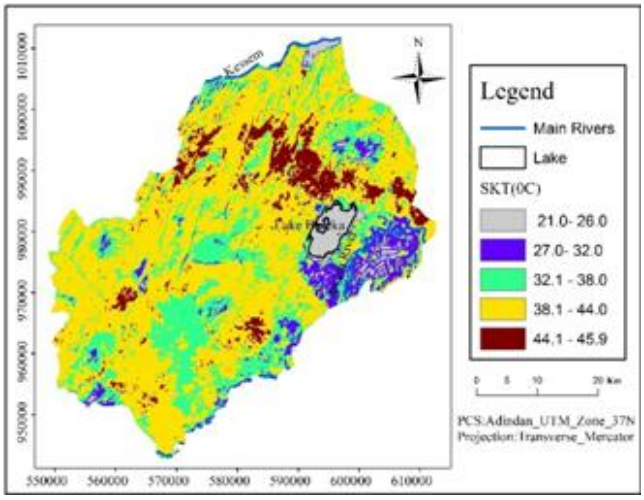

Figure 6: Surface kinetic temperature map of the study area

4.1.4 Validation of Surface Kinetic Temperature

The consistency of surface kinetic temperature results from TIRS sensors may not always be validated with ground surface temperature due to the non-availability of field data alongside satellite overpass [19]. In this study, daytime average 8-day per-pixel LST products of MODIS (MOD11A2) with a 1-kilometer spatial resolution was used within the period of 09/01/2019 to 16/01/2019 for comparison and validation of surface kinetic temperature. The 8-day compositing period was selected since twice that period is the exact ground track repeat period of the Terra and Aqua platforms. The Landsat 8 surface kinetic temperature results with the 30-meter spatial resolution were resampled using bilinear interpolation technique to 1kilometer spatial resolution to match with MODIS LST products. The statistical comparison was done by taking 13 points at any spatial location of both resampled surface kinetic temperature thematic layer and MODIS LST product using random sampling techniques. The surface temperature comparison between Landsat 8 TIRS and MODIS LST product has a maximum difference of 2^0C [61, 73, 74]. Based on our statistical analysis done on both surface temperature products, the Root Mean Square Error was 1.75 ^{0}C as shown in table (2) and the result was consistent and the accuracy of surface kinetic temperature retrieved from Landsat 8 OLI and TIR sensor data was found in an acceptable range. The spatial correlation of surface temperature product was shown in figure (7).

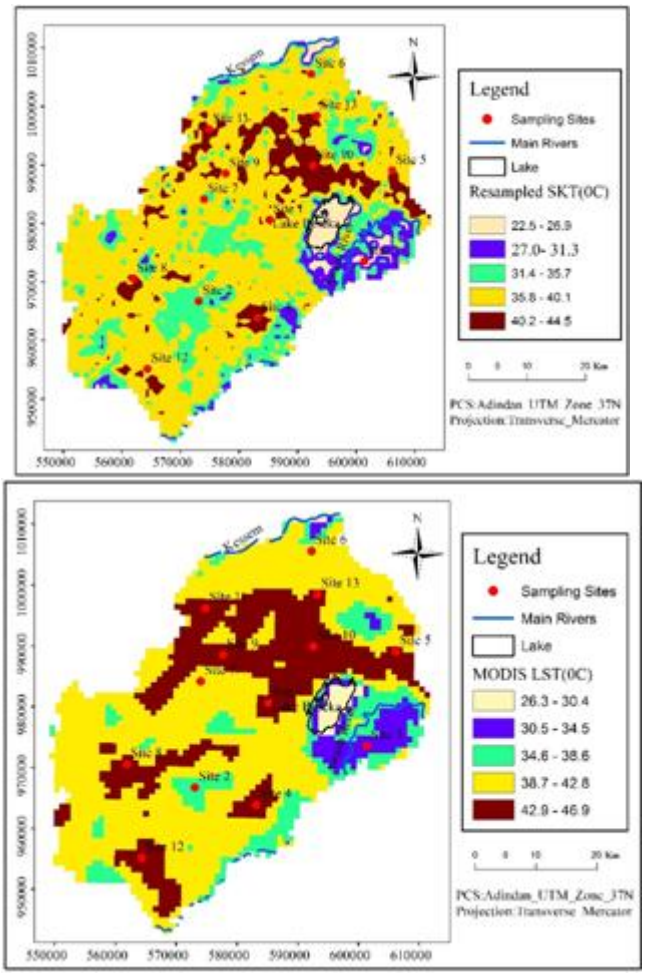

Figure 7: Resampled Landsat 8(A) and MOD11A2 (B) with 1km spatial resolution

Table 2: Statistical comparison of MODIS LST and resampled Lands at 8 surface temperature

Sampling sites	MODIS LST(M) in ^{0}C	Landsat8 SKT(L) in ^{0}C	M-L in ^{0}C	(M-L)2 in ^{0}C
Site 1	44.05	43.42	0.6	0.36
Site 2	37.69	37.71	-0.02	0.0004
Site 3	31.01	28.26	2.75	7.56
Site 4	43.71	42.32	1.39	1.93
Site 5	42.95	42.98	-0.03	0.0009
Site 6	39.97	39.29	0.68	0.46
Site 7	41.67	39.67	2	4
Site 8	43.51	41.88	1.63	2.66
Site 9	44.49	42.80	1.69	2.85
Site 10	45.89	43.16	2.73	7.45
Site 11	44.39	43.38	1.01	1.02
Site 12	44.49	41.74	2.75	7.56
Site 13	44.25	42.22	2.03	4.12
Sum of (M-L)2				39.97
(Sum/Total sample)				3.07
Square root(Sum/Total sample)				1.75

4.1.5 Suitability Analysis of Geothermal Potential Fields

The geothermal potential field was detected based on the classified evidence layers of surface kinetic temperature anomaly spatially distributed over the study area as shown in figure (8). The surface kinetic temperature thematic layer was classified as highly suitable, suitable, moderately

suitable, less suitable and unsuitable classes based on their values, as indicated in table (3) [18, 58].

Table 3: Surface Kinetic Temperature classification (SKT)

SKT in ^{0}C	Rank	Suitability	Area(Km^2)
<26	1	Unsuitable	77.24
27-32	2	Less suitable	155.41
33-38	3	Moderately suitable	580.38
39-44	4	Suitable	1439.57
>44	5	Highly suitable	184.21

The analysis of geothermal potential suitability indicated that a highly suitable geothermal field was mainly found in Fantale prospect area located around in between Kone and Fantale volcano as shown in figure(8). There is also a potential area south of Kone volcano, near to Bosetti volcano at the southwestern tip of the study area, north of Borchota towns and along the northeastern-southwestern direction of the study area following the rift axis of the Main Ethiopian Rift. Based on the result of our analysis, Fantale geothermal prospect area shows noticeable geothermal potential sites that could be feasible for geothermal power plant installation as compared to Kone geothermal prospect area and Boseti volcano areas as shown in figure (9).

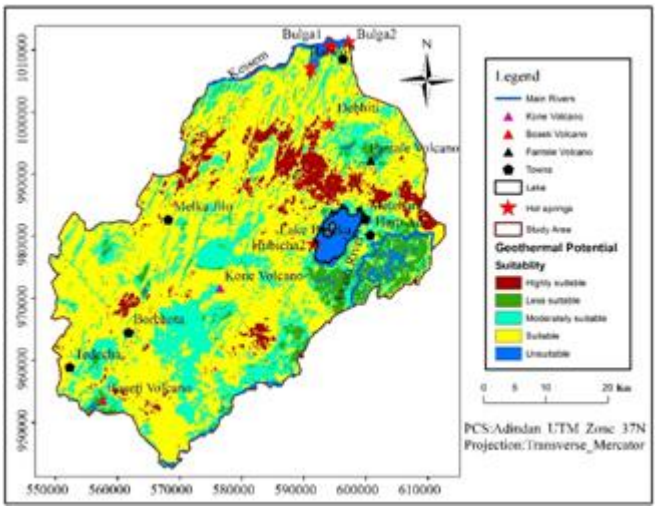

Figure 8: Geothermal potential map

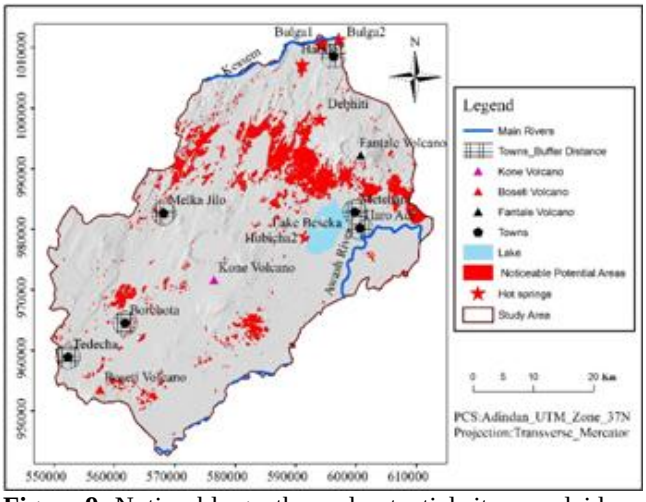

Figure 9: Noticeable geothermal potential sites overlaid on hill shade

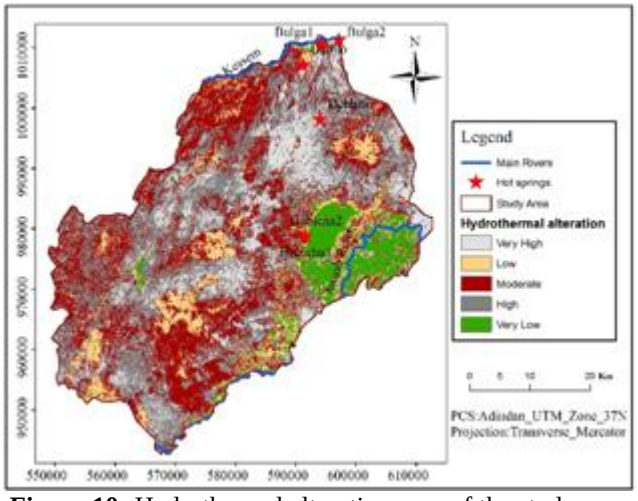

Figure 10: Hydrothermal alteration map of the study area

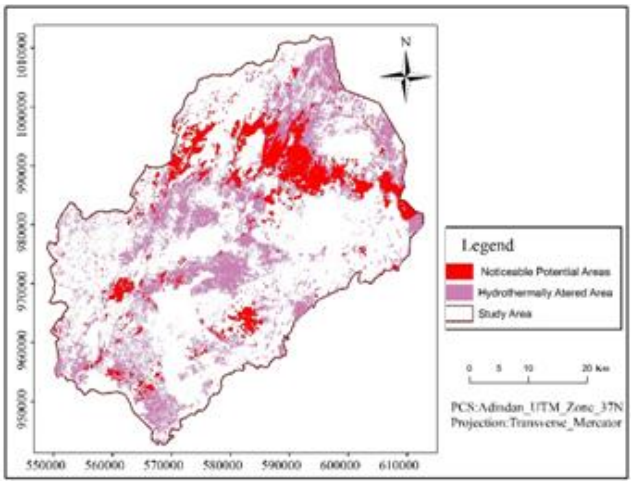

Figure 11: Higher surface temperature anomalies compared with altered grounds

4.2 Discussions

In this study, higher surface kinetic temperature anomaly areas which has a temperature above 44 ^{0}C were selected for noticeable geothermal potential sites. As per the results of this study, most of the potential areas were found in Fantale geothermal prospect area in which concentrated thermal manifestations in the form of hot springs, fumaroles, altered and steaming grounds and mud pools were found [9,15,38,76,78]. The results of this study indicate geothermal potential sites at Habilo-Tedecha,Hubicha, Kessem River and Fantale volcano areas which are active hydrothermal fields and is found in Fantale geothermal prospect areas. Previous studies also showed Fantale volcano area as one of the active hydrothermal fields in the study site [9, 15]. Hydrothermal activities were observed in different parts of Fantale area. The most extensive and essential hydrothermal active surface manifestations were located around Melka-Tedecha area mostly northeast of Melka Jilo town as shown in figure (8). This area has been characterized by several hot springs, mud pools, fumaroles, and a wide area of altered and steaming grounds which has changed the color of pumice to red [60]. Most of the area has satellite measured surface kinetic temperature above 44 ^{0}C as displayed in figure (6). Hubicha areas hydrothermal fields are located south of Fantale volcano on the southwestern shore of Lake Beseka (figure 8). The area has many hot springs and

discharge into the lake with a satellite measured temperature above 39 ^{0}C. They originate at the base of recently faulted basalt running 20^0 north-northeast direction. There is also a running deep fissure close to the hot springs. There are many hot springs along this fault currently covered by the expansion of Lake Beseka [9, 60, 76]. Kessem River areas hydrothermal fields are located at the northern tip of the study area following Kessem River as shown in figure 8 and northeast of Tedecha fumaroles on the southern band of Kessem River [9,60,76]. This area has many hot springs. Most of these areas have a satellite measured surface kinetic temperature of 40 ^{0}C. Furthermore, Habilo-Tedecha areas hydrothermal fields are located northwest of Fantale volcano close to the western escarpment (figure 8). The area has several hot springs, mud pools, fumaroles, and a wide area of altered and steaming grounds [9, 60, 76].

Since the study area is located in the northern sector of the Main Ethiopian Rift, it is characterized by active extensional tectonic movement, the relative movement extended about 6 to 7mm/year between the African and Somalian plates [11, 16, 24]. Due to this reason, the area is well known in Quaternary volcano-tectonic deformation in terms of seismic, structure, and geodetic data [1, 3, 4, 11,40.50, 68, 87, 88]. The northern Main Ethiopian Rift is also affected by two normal fault systems namely: the border faults and a set of faults affecting the rift floor, usually referred to as Wanji Fault Belt [87, 88]. The border faults are normally long, widely spaced, and characterized by large vertical offset and are understood to have accommodated the tectonic deformation during the initial stages of rifting [88]. However, the Wanji Fault Belt is an active volcano-tectonic system characterized by short, closely spaced, active faults that exhibit minor vertical throw which developed essentially in the last 2 million years ago [3, 4,87, 88]. The crust is thinning in the northern segment along the rift axis towards the Afar Depression [88]. The study area has two magmatic segments namely: Boseti-Kone and Dofan-Fantale magmatic segments which have a significant amount of geothermal potential [12].

The Dofan-Fantale magmatic segments was characterized by recent summit caldera collapse felsic lava extrusions in the caldera floor and the appearance of widespread fumarolic activity signifying the existence of a shallow magma chamber and active tensional tectonics fissures up to 2 meters wide [3, 4]. Therefore, the area has a significant amount of geothermal resources as compared to Boseti-Kone magmatic segment. The outcomes of the previous study suggested that Dofan-Fantale geothermal prospect areas are potentially prospective for detail geothermal exploration [9, 15, 38, 76, 78]. The results of this study also confirmed that most of the noticeable geothermal potential sites were found in Fantale geothermal prospects, which is located in Dofan-Fantale magmatic segment. Some of the volcano areas in Boseti-Kone magmatic segment have shown higher surface temperature anomalies. In this area, a series of volcanic domes, cones, calderas and craters were found following the Main Ethiopian Rift axis and specifically volcanic domes and cones regions have shown higher surface temperature anomalies. Moreover, during our field investigation, we have confirmed that higher surface temperature anomalies were found in the nearby locations of concentrated spatial distribution of hot springs, fumaroles, mud pools, and steaming ground that are standard thermal manifestations in the great East African Rift Valley [10]. These thermal manifestations are closely associated with Quaternary volcanoes in the axis of the rift. The association is related to shallow hot magma bodies under the massifs which are heat sources [55].

Altered rocks are one of the major geothermal surface manifestation parameters [37]. Mapping of hydrothermally altered rocks and associated mineralization is essential in geothermal exploration [46]. These altered rocks are mapped through the spectral characteristics of the Lands at 8 satellite sensor in visible and near-infrared spectral resolution [44,46]. The detection of the locations and spatial distribution of hydrothermal alteration zones can assist in identifying geothermal potential areas as alteration zones are closely associated with geothermal heat flow from the interior to the surface of the Earth's crust [2, 5]. Figure 10 shows hydrothermal alteration of rocks and associated minerals. The highest geothermal potential occurs within and around hydrothermal alteration zones as compared to unaltered areas. Comparing higher surface kinetic temperature anomaly area with hydrothermally altered grounds in figure [11], shows highly spatial correlations between higher thermal anomaly and hydrothermally altered areas. The highest surface temperature anomalies areas show higher alteration while lowest surface temperature anomalies areas show lower alterations.

This study shows that Landsat 8 OLI and TIRS sensors data can effectively determine the surface kinetic temperature for a large geographic area and find out noticeable geothermal potential sites, indicating the importance of Landsat 8 imagery for geothermal potential exploration. Previous studies also used Lands at imagery for geothermal exploration [13, 17, 19, 31, 61, 63, 82]. However, these studies failed to consider the amount of energy radiated from the objects that depend on land surface emissivity and kinetic temperature of the objects. In our study, we used the Emissivity modulation method to retrieve surface kinetic temperature of the objects from Lands at 8 OLI and TIR sensors. The radiant and surface kinetic temperature retrieved from satellite images for thermal mapping is relative to actual surface temperature [59]. The radiant temperature estimated from remote sensing data is always less than the actual surface temperature of the body by the factor of emissivity (e) the power of 0.25 [8,59]. The results of his study indicated that surface kinetic temperature is used to identify geothermal fields and hydrothermal activities over the study area. This indicates that an emissivity modulation method is an effective, accurate and appropriate method to estimate the actual surface temperature of the objects from satellite imagery for geothermal exploration. Moreover, this study considered artificial thermal influences as false geothermal anomalies, as shown in figure (9), a 2000meter buffer distance from the towns was made to minimize the effect of rising temperature due to urbanization [19].

5. Conclusion

Lands at 8 imagery of thermal infrared band 10 and operational land imagery (OLI bands) are used to retrieve surface kinetic temperature using the Emissivity Modulation (EM) method and resulted with minimum and maximum values of 21 and 45.9 ^{0}C respectively. This surface kinetic temperature is reclassified into some categories to identify geothermal potential areas. The highest surface temperature anomalies indicated that the occurrence of high geothermal heat reservoirs at shallow depths and is considered as highly suitable areas. The lowest surface temperature anomalies indicate the occurrence of low geothermal heat reservoirs at shallow depths and are considered as unsuitable. However, the surface temperature is affected by land cover types, land surface emissivity and thermal properties of the materials. The highest surface temperature anomalies are found in the region of highly faulted areas, in silicic volcanic domes areas following the rift axis of the Main Ethiopian Rift Valley, in the location of hot springs, fumaroles, mud pools and hydrothermally altered rocks. Therefore, most of the geothermal potential areas are found in Fantale geothermal prospect areas and less pronounced geothermal potential areas are found in Kone volcanic complex and Boseti volcano. Based on fieldwork investigation and the result of this study, Fantale geothermal prospects areas has economically important geothermal energy resource. This study showed the contribution of remote sensing technology for an effective potential geothermal site identification. Furthermore, remote sensing techniques have a vital role in geothermal energy development project programs since it can map previously unmapped geothermal prospect areas. Hence, remote sensing satellite data are found to be useful for qualitatively and quantitatively analyzing geothermal resource potential areas.

References

[1] Abebe T., Manetti P., Bonini M., Corti G., Innocenti F., Mazzarini F. (2005). Geological Map (Scale 1:200 000) of the Northern Main Ethiopian Rift and its Implication for the Volcano-Tectonic Evolution of the Rift. Geological Society of America Maps and Charts.

[2] Abubakar, A. J., Hashim, M., & Pour, A. B. (2018). Evaluation and Detection of Geothermal Potential Zones in Yankari Park, South-Central Part of Bauchi State, North-Eastern Nigeria. Journal of Applied Sciences and Environmental Management, 22(9), 1381-1385.

[3] Agostini A., Bonini M., Corti G., Sani F., Manetti P. (2011a). Distribution of Quaternary Deformation in the Central Main Ethiopian Rift, East Africa. Tectonics, 30.

[4] Agostini A., Bonini M., Corti G., Sani F., Mazzarini F. (2011b). Fault Architecture in the Main Ethiopian Rift and Comparison with Experimental Models: Implications for Rift Evolution and Nubia-Somalia Kinematics. Earth and Planetary Science Letters, 301, 479-492.

[5] Ahmed, A. (2020). Hydrothermal Alteration Mapping for Geothermal Exploration in Manda-Inakir Area, NW of the Republic of Djibouti, 1–9.

[6] Asrat, D. A. (2005). Introduction to Physical Geology. Addis Ababa University, 1–277.

[7] Avdan, U., & Jovanovska, G. (2016). Algorithm for Automated Mapping of Land Surface Temperature Using Landsat 8 Satellite Data. Journal of Sensors.

[8] Ayenew, T. (2001). Surface Kinetic Temperature Mapping Using Satellite Spectral Data in Central Main Ethiopian Rift and Adjacent Highlands. SINET: Ethiopian Journal of Science, 24(1), 51-68.

[9] Bekele, B., Mamo, T., Teclu, A., & Kebede, Y. (2007). Compilation of the Geoscientific Study of the Dofan-Fantale Geothermal Prospect, Ethiopia.

[10] Bertani, R., Cavadini, M., & Everett, M. (2018). Geothermal Power Opportunities in the Rift Valley.

[11] Bonini, M., Corti, G., Innocenti, F., Manetti, P., Mazzarini, F., Abebe, T., & Pecskay, Z. (2005). Evolution of the Main Ethiopian Rift in the frame of Afar and Kenya Rifts Propagation. Tectonics, 24(1).

[12] Boone S.C., Balestrieri M.L., Kohn B.P., Corti G., Gleadow A.J.W., Seiler C. (2019). Tectono-Thermal Evolution of the Broadly Rifted Zone, Ethiopian Rift. Tectonics, 38, 1070–1100.

[13] Chan, H. P., Chang, C. P., & Dao, P. D. (2018). Geothermal Anomaly Mapping Using Landsat ETM+ Data in Ilan Plain, Northeastern Taiwan. Pure and Applied Geophysics, 175(1), 303-323.

[14] Chander, G., Markham, B. L., & Helder, D. L. (2009). Summary of Current Radiometric Calibration Coefficients for Landsat MSS, TM, ETM+, and EO-1 ALI Sensors. Remote Sensing of Environment, 113(5), 893-903.

[15] Chernet, T. (2005). Geological and Hydrothermal Alteration Mapping of the Dofan Geothermal Prospect and Adjacent Western Escarpment (Ethiopia). In *Proceedings of the World Geothermal Congress, Antalya, Turkey*, pp. 24-29.

[16] Chu, D., and R. G. Gordon (1999), Evidence for Motion between Nubia and Somalia along the Southwest Indian Ridge, Nature, 398, 64 – 67.

[17] Coolbaugh, M.F.; Kratt, C.; Fallacaro, A.; Calvin, W.M.; Taranik, J.V. (2007). Detection of Geothermal Anomalies Using Advanced Spaceborne Thermal Emission And Reflection Radiometer (ASTER) Thermal Infrared Images at Bradys Hot Springs, Nevada, USA. Remote Sens. Environ. 106, 350–359.

[18] D P Cesarian, I A Abir and M Isa (2018). Comparison of In-Situ Temperature and Satellite Retrieved Temperature in Determining Geothermal Potential in Jaboi Field, Sabang. Journal of Physics.

[19] Darge, Y. M., Hailu, B. T., Muluneh, A. A., & Kidane, T. (2019). Detection of Geothermal Anomalies Using Landsat 8 TIRS Data in Tulu Moye Geothermal Prospect, Main Ethiopian Rift. International Journal of Applied Earth Observation and Geoinformation, 74, 16-26.

[20] Dickson MH and Fanelli M. (2004). What is geothermal energy? Pisa, Italy: Istituto di Geoscienze e Georisorse, CNR.

[21] DiPippo, R. (2012). Geothermal Well Drilling. Geothermal Power Plants. Elsevier,39–47.

[22] Eneva, M. (2010). Geothermal Exploration in Eastern California Using ASTER Thermal Infrared Data: Final Project Report. California Energy Commission.

[23] ENVI (2009). Atmospheric Correction Module: QUAC and FLAASH 'User's Guide. Version, 4, 44.
[24] Fernandes, R. M. S., B. A. C. Ambrosius, R. Noomen, L. Bastos, L. Combinck, J. M. Miranda, and W. Spakman (2004), Angular Velocities of Nubia and Somalia from Continuous GPS Data:Implications on Present-Day Relative Kinematics, Earth Planet. Sci. Lett., 222, 197 – 208.
[25] FIG (2010). Geothermal Technologies Program. Office of Energy Efficiency and Renewable Energy, US Department of Energy.
[26] Fridleifsson, I.B.; Bertani, R.; Huenges, E.; Lund, J.W.; Ragnarsson, A.; Rybach, L.(2008). The Possible Role and Contribution of Geothermal Energy to the Mitigation of Climate Change. In Proceedings of The IPCC Scoping Meeting on Renewable Energy Sources, Lübeck, Germany, 59–80.
[27] Gaudin, D., Beauducel, F., Allemand, P., Delacourt, C., & Finizola, A. (2013). Heat Flux Measurement from Thermal Infrared Imagery in Low-Flux Fumarolic Zones: Example of the Ty Fault (La Soufrie`Re De Guadeloupe). Journal of Volcanology and Geothermal Research, 267, 47–56.
[28] Gutie´rrez, F. J., Lemus, M., Parada, M. A., Benavente, O. M., & Aguilera, F. A. (2012). Contribution of Ground Surface Altitude Difference to Thermal Anomaly Detection Using Satellite Images: Application to Volcanic/Geothermal Complexes in the Andes of Central Chile. Journal of Volcanology and Geothermal Research, 237–238, 69–80.
[29] Haselwimmer, C., & Prakash, A. (2013). Thermal Infrared Remote Sensing of Geothermal Systems. In Thermal Infrared Remote Sensing Springer, Dordrecht, Netherlands,17, 453–473.
[30] Hashim, H., Abd Latif, Z., & Adnan, N. A. (2019). Urban Vegetation Classification with NDVI Threshold Value Method with Very High Resolution (VHR) PLEIADES Imagery. Int. Arch. Photogramm. Remote Sens. Spat. Inf. Sci, 237-240.
[31] Hodder, D.T. (1970). Application of Remote Sensing to Geothermal Prospecting. Geothermics 2, 368–380.
[32] Howari, F. (2015). Prospecting for Geothermal Energy Through Satellite Based Thermal Data: Review and the Way Forward. Glob. J. Environ. Sci. Manag. 1, 265–274.
[33] Hui, L., Qing-jun, Z., Puyuan, T., & Wen-guang, H. (2015). Technologies and Applications of Geophysical Exploration in Deep Geothermal Resources in China.
[34] Ientilucci, E. J. (2007). Using MODTRAN Predicting Sensor-Reaching Radiance. Chester F. Carlson Center for Imaging Science and Rochester Institute of Technology.
[35] Jiménez-Muñoz, J. C., Sobrino, J. A., Skoković, D., Mattar, C., & Cristóbal, J. (2014). Land Surface Temperature Retrieval Methods from Landsat-8 Thermal Infrared Sensor Data. IEEE Geoscience and Remote Sensing Letters, 11(10), 1840-1843.
[36] Kabeyi, M. J. B. (2019). Geothermal Electricity Generation, Challenges, Opportunities and Recommendations. International Journal of Advances in Scientific Research and Engineering, 5(8), 53-95.
[37] Kandie, R., Kubai, R., Mwania, M., Okech, E., & Omiti, A. (2014). Structural Geology Field Mapping of the Eburru-Badlands Geothermal Prospect. Kengen Internal Report.
[38] Kebede, S. (2012). Geothermal Exploration and Development in Ethiopia: Status and Future Plan. Short Course VII on Exploration for Geothermal Resources Organized by UNU-GTP, GDC and KenGen.
[39] Kebede, S. (2014). Opportunities and Challenges in Geothermal Exploration and Development in Ethiopia. Transactions - Geothermal Resources Council, 38(Ii), 589–591.
[40] Keranen, K., & Klemperer, S. L. (2008). Discontinuous and Diachronous Evolution of the Main Ethiopian Rift: Implications for Development of Continental Rifts. Earth and Planetary Science Letters, 265(1-2), 96-111.
[41] Kuenzer, C., & Dech, S. (2013). Theoretical Background of Thermal Infrared Remote Sensing. In Thermal Infrared Remote Sensing, Springer, Dordrecht, 1-26.
[42] Lago González, D., & Rodríguez-Gonzálvez, P. (2019). Detection of Geothermal Potential Zones Using Remote Sensing Techniques. *Remote Sensing*, *11*(20), 2403.
[43] Macharia, M.W.; Gachari, M.K.; Kuria, D.N.; Mariita, N.O. (2017). Low Cost Geothermal Energy Indicators and Exploration Methods in Kenya. J. Geogr. Reg. Plan. 10, 254–265.
[44] Mahboob, M. A., Genc, B., Celik, T., Ali, S., & Atif, I. (2019). Mapping Hydrothermal Minerals Using Remotely Sensed Reflectance Spectroscopy Data from Landsat. Journal of the Southern African Institute of Mining and Metallurgy, 119(3), 279-289.
[45] Marini L. (2001). Geochemical Techniques for the Exploration and Exploitation of Geothermal Energy. Italy: University of Genua.
[46] Mia, M., Fujimitsu, Y., & Nishijima, J. (2018). Monitoring Thermal Activity of the Beppu Geothermal Area in Japan Using Multisource Satellite Thermal Infrared Data. Geosciences, 8(8), 306.
[47] Moran, M.S. (1995).Thermal remote sensing, Agricultural and Forest Meteorology, 77(3–4), 5-7.
[48] Muluneh A.A., Kidane T., Corti G., Keir D. (2018). Constraints on Fault and Crustal Strength of the Main Ethiopian Rift from Formal Inversion of Earthquake Focal Mechanism Data. Tectonophysics, 731-732, 172-180.
[49] Negawo, W.J. (2016). A Review on the Geomaterial Aspects of Geothermal Reservoirs and Its Exploration. Journal of Environment and Earth Science, 6, 229-238.
[50] Nichol, J. (2009). An Emissivity Modulation Method for Spatial Enhancement of Thermal Satellite Images in Urban Heat Island Analysis. Photogrammetric Engineering & Remote Sensing, 75(5), 547-556.
[51] Nichol, J. E. (1994). A GIS-Based Approach to Microclimate Monitoring in Singapore's High-Rise Housing Estates. Photogrammetric Engineering and Remote Sensing, 60(10), 1225-1232.
[52] Nugroho, U. C., & Domiri, D. D. (2017). Identification of Land Surface Temperature Distribution of Geothermal Area in Ungaran Mount by Using Landsat 8 Imagery. International Journal of Remote Sensing and Earth Sciences (IJReSES), 12(2), 143-150.

[53] Omenda, P. A. (2009). The Geothermal Activity of the Past East African Rift.
[54] Omwenga, B. M. Geothermal Well Site Suitability Selection Using Geographic Information Systems (GIS) and Remote Sensing: Case Study of the Eburru Geothermal Field.
[55] Ourhzif, Z., Algouti, A., & Hadach, F. (2019). Lithological Mapping Using Landsat 8 OLI and ASTER Multispectral Data in Imini-Ounilla District South High Atlas of Marrakech. International Archives of the Photogrammetry, Remote Sensing and Spatial Information Sciences.
[56] Pastor, M. S. (2010). Application of Thermal Remote Sensing for Geothermal Mapping, Lake Naivasha, Kenya. World Geothermal Congress Bali, Indonesia.
[57] Prakash, A. (2000). Thermal Remote Sensing: Concepts, Issues and Applications. International Archives of Photogrammetry and Remote Sensing, 33(B1; PART 1), 239-243.
[58] Pürschel, M., Gloaguen, R., & Stadler, S. (2013). Geothermal Activities in the Main Ethiopian Rift: Hydrogeochemical Characterization of Geothermal Waters and Geothermometry Applications (Dofan-Fantale, Gergede-Sodere, Aluto-Langano). Geothermics, 47, 1-12.
[59] Qin, Q.; Zhang, N.; Nan, P.; Chai, L. (2011). Geothermal Area Detection Using Landsat ETM+ Thermal Infrared Data and Its Mechanistic Analysis: A Case Study in Tengchong, China. Int. J. Appl. Earth Obs. Geoinf. 13,552–559.
[60] Sadeghi B. and Khalajmasoumi M. (2014). A Futuristic Review for Evaluation of Geothermal Potentials Using Fuzzy Logic and Binary Index Overlay in GIS Environment. Renewable and Sustainable Energy Reviews, 43 (2015), 818–831.
[61] Seielstad, C., Queen, L. (2009). Thermal Remote Monitoring of the Norris Geyser Basin, Yellowstone National Park. Unpublished technical report. Yellowstone National Park, USA.
[62] Sekertekin A. and Arslan N. (2019). Monitoring Thermal Anomaly and Radiative Heat Flux Using Thermal Infrared Satellite Imagery: A Case Study at Tuzla Geothermal Region. Geothermics, 78, 243-254.
[63] Sekertekin, A., and Bonafoni, S. (2020). Land Surface Temperature Retrieval from Landsat 5, 7, And 8 Over Rural Areas: Assessment of Different Retrieval Algorithms and Emissivity Models and Toolbox Implementation. Remote Sensing, 12(2), 294.
[64] Shah, R. R., & Dutt, B. (2014). Geothermal Energy : An Alternative Source of Energy. Journal of Engineering Research and Applications, 4(4), 63–68.112.
[65] Sholihah, R. I., & Shibata, S. (2019). Retrieving Spatial Variation of Land Surface Temperature Based on Landsat OLI/TIRS: A Case of Southern Part of Jember, Java, Indonesia. In IOP Conference Series: Earth and Environmental Science, 362(1).
[66] Siegburg M. Bull J.M., Nixon C.W., Keir D., Gernon T.M., Corti G., Bekele Abebe B., Sanderson D.J., Ayele A. (2020). Quantitative Constraints on Faulting and Fault Slip-Rates in the Northern Main Ethiopian Rift. Tectonics, 39.
[67] Skoković, D., Sobrino, J. A., Jimenez-Munoz, J. C., Soria, G., Julien, Y., Mattar, C., & Cristóbal, J. (2014). Calibration and Validation of Land Surface Temperature for Landsat 8-TIRS Sensor. Land Product Validation and Evolution.
[68] Sobrino, J. A., & Raissouni, N. (2000). Toward Remote Sensing Methods for Land Cover Dynamic Monitoring: Application to Morocco. International Journal of Remote Sensing, 21(2), 353-366.
[69] Sobrino, J. A., Jiménez-Muñoz, J. C., & Paolini, L. (2004). Land Surface Temperature Retrieval from Landsat TM 5. Remote Sensing of Environment, 90(4), 434-440.
[70] Sobrino, J. A., Jiménez-Muñoz, J. C., Sòria, G., Romaguera, M., Guanter, L., Moreno, J., & Martínez, P. (2008). Land Surface Emissivity Retrieval from Different VNIR and TIR Sensors. IEEE Transactions on Geoscience and Remote Sensing, 46(2), 316-327.
[71] Srivastava, P. K., Majumdar, T. J., and Bhattacharya, A. K. (2009). Surface Temperature Estimation in Singhbhum Shear Zone of India Using Landsat-7 ETM+ Thermal Infrared Data. Advances in Space Research, 43(10), 1563-1574.
[72] Srivastava, P. K., Majumdar, T. J., and Bhattacharya, A. K. (2010). Study of Land Surface Temperature and Spectral Emissivity Using Multi-Sensor Satellite Data. Journal of Earth System Science, 119(1), 67-74.
[73] Taqiuddin, Z. M., Nordiana, M. M., & Rosli, S. (2016). Utilizing of Geophysical Method for Geothermal Exploration in Acehbesar (Indonesia). International Research Journal of Engineering and Technology, 3(4), 2234–2238.
[74] Teclu, A. (2005). Geochemical and Isotopic Study of Dofan-Fantale Geothermal Prospect.
[75] Tefera, M., Chernet, T., & Har, W. (1996). Explanation of the Map. Realities of Irish Life, 363–366.
[76] Teklemariam, M., & Beyene, K. (2005). Geothermal Exploration and Development in Ethiopia. Short Course VII on Exploration for Geothermal Resources, 24–29.
[77] Teklemariam, M., Beyene, K., AmdeBerhan, Y., & Gebregziabher, Z. (2000). Geothermal Development in Ethiopia. In *Proceedings, World Geothermal Congress*, 475-480.
[78] Tommasini S., Manetti P., Innocenti F., Abebe T., Sintoni M.F., Conticelli S. (2005). The Ethiopian Subcontinental Mantle Domains: Geochemical Evidence from Cenozoic Mafic Lavas. Mineralogy and Petrology, 84,259-281.
[79] USGS. (2019). Landsat 8 Data Users Handbook.
[80] Van der Meer, F.D.; Van der Werff, H.M.A.; Van Ruitenbeek, F.J.A. (2014) Potential of ESA's Sentinel-2 for Geological Applications. Remote Sens. Environ. 148, 124–133.
[81] Vlassova, L., Perez-Cabello, F., Nieto, H., Martín, P., Riaño, D., & De La Riva, J. (2014). Assessment of Methods for Land Surface Temperature Retrieval from Landsat-5 TM Images Applicable to Multiscale Tree-Grass Ecosystem Modeling. Remote Sensing, 6(5), 4345-4368.
[82] Wu, W., Zou, L., Shen, X., Lu, S., Su, N., Kong, F., et al. (2012). Thermal Infrared Remote-Sensing

Detection of Thermal Information Associated with Faults: A Case Study in Western Sichuan Basin, China. Journal of Asian Earth Sciences, 43, 110–117.

[83] Yousefi H, Noorollahi Y, Ehara S, Itoi R, Yousefi A. and Fujimitsu Y, et al.(2010). Developing the Geothermal Resources Map of Iran. Geothermics.39:140–51.

[84] Yu, X., Guo, X., & Wu, Z. (2014). Land Surface Temperature Retrieval from Landsat 8 TIRS-Comparison between Radiative Transfer Equation-Based Method, Split Window Algorithm and Single Channel Method. Remote Sensing, 6(10), 9829-9852.

[85] Zwaan F., Corti G., Keir D., Sani F. (2019). A Review of Tectonic Models for the Rifted Margin of Afar: Implications for Continental Break-Up and Passive Margin Formation. Journal of African Earth Sciences, 164, 103649, 1-22.

[86] Zwaan F., Corti G., Sani F., Keir D., Muluneh A., Illsley-Kemp F. Papini M. (2020). Structural Analysis of the Western Afar Margin, East Africa: Evidence for Multiphase Rotational Rifting. Tectonics, 39.